Title

Uncovering matrix effects on lipid analyses in MALDI imaging mass spectrometry experiments.

Journal

Journal of Mass Spectrometry, 55(4)

Authors

Perry, William

Patterson, Nathan

Prentice, Boone

et al.

Publication Date

2020-04-01

DOI

10.1002/jms.4491

Peer reviewed

Published in final edited form as:

J Mass Spectrom. 2020 April ; 55(4): e4491. doi:10.1002/jms.4491.

Uncovering Matrix Effects on Lipid Analyses in MALDI Imaging Mass Spectrometry Experiments

William J. Perry[1,2], **Nathan Heath Patterson**[1,3], **Boone M. Prentice**[1,3], **Elizabeth K. Neumann**[1,3], **Richard M. Caprioli**[1,2,3,4,5], **Jeffrey M. Spraggins**[1,2,3,‡]

[1]Mass Spectrometry Research Center, Vanderbilt University, Nashville, TN

[2]Department of Chemistry, Vanderbilt University, Nashville, TN

[3]Department of Biochemistry, Vanderbilt University, Nashville, TN

[4]Department of Pharmacology, Vanderbilt University, Nashville, TN

[5]Department of Medicine, Vanderbilt University, Nashville, TN

Abstract

The specific matrix used in matrix-assisted laser desorption/ionization imaging mass spectrometry (MALDI IMS) can have an effect on the molecules ionized from a tissue sample. The sensitivity for distinct classes of biomolecules can vary when employing different MALDI matrices. Here, we compare the intensities of various lipid sub-classes measured by Fourier transform ion cyclotron resonance (FT-ICR) IMS of murine liver tissue when using 9-Aminoacridine (9AA), 5-Chloro-2-mercaptobenzothiazole (CMBT), 1,5-Diaminonaphthalene (DAN), 2,5-Dihydroxyacetophenone (DHA), and 2,5-Dihydroxybenzoic acid (DHB). Principal component analysis and receiver operating characteristic curve analysis revealed significant matrix effects on the relative signal intensities observed for different lipid sub-classes and adducts. Comparison of spectral profiles and quantitative assessment of the number and intensity of species from each lipid sub-class showed that each matrix produces unique lipid signals. In positive ion mode, matrix application methods played a role in the MALDI analysis for different cationic species. Comparisons of different methods for the application of DHA showed a significant increase in the intensity of sodiated and potassiated analytes when using an aerosol sprayer. In negative ion mode, lipid profiles generated using DAN were significantly different than all other matrices tested. This difference was found to be driven by modification of phosphatidylcholines during ionization that enables them to be detected in negative ion mode. These modified phosphatidylcholines are isomeric with common phosphatidylethanolamines confounding MALDI IMS analysis when using DAN. These results show an experimental basis of MALDI analyses when analyzing lipids from tissue and allow for more informed selection of MALDI matrices when performing lipid IMS experiments.

‡ Corresponding Author Address reprint requests to Jeffrey M. Spraggins, V9140 MRBIII, 465 21st Ave South, Nashville, TN 37232, (615) 343-7333, jeff.spraggins@vanderbilt.edu.

Keywords

MALDI IMS; matrix-assisted laser desorption/ionization mass spectrometry; Imaging mass spectrometry; MALDI matrix; lipid imaging

Introduction

Matrix-assisted laser desorption/ionization (MALDI) utilizes a small, organic chemical matrix that aids in analyte desorption and ionization [1]. In MALDI imaging mass spectrometry (IMS), ions are generated from discrete x,y locations (pixels) across a sample surface using laser irradiation, and a mass spectrum is recorded at each position. Ion images are visualized by plotting the relative abundance of any mass-to-charge ratio (*m/z*) as a heat map over the measurement area [2–4]. No current MALDI matrix preparation provides high sensitivity for all classes of biomolecules within a single IMS experiment. Thus, the MALDI matrix chosen for an IMS experiment will greatly influence the measured intensities of various analyte classes during analysis [5].

MALDI matrices are chosen based on their ability to provide sufficient ionization efficiency for a given analyte class (*e.g.* low molecular weight metabolites, lipids, proteins, polymers, or inorganic compounds) or sub-class [6–13]. Differences in observed analyte sensitivities can be attributed to the physical properties of a matrix such as molecular structure, pH, proton affinity, and peak wavelength absorbance [12–18]. 2,5-Dihydroxybenzoic acid (DHB) is the most widely employed and studied MALDI matrix offering sufficient sensitives for many analyte classes in positive ion mode MS analysis [16, 19–23]. 9-Aminoacridine (9AA) is often used for the analysis of low molecular weight compounds in negative ion mode MS analysis and 1,5-Diaminonaphthalene (DAN) ionizes many sub-classes of lipid species with high sensitivity in both polarities [12, 18]. While both 9AA and DAN are considered sensitive matrices, energy transferred during the MALDI process can result in analyte modification or fragmentation complicating data interpretation [19, 24, 25]. Volatility is also a consideration when selecting a MALDI matrix because the matrix layer must remain stable for lengthy acquisition times (hours) to avoid signal loss during an imaging experiment. Matrix sublimation becomes a concern when using instruments with high vacuum source regions. 2,5-Dihydroxyacetophenone (DHA) is an excellent matrix for MS analysis of multiple analyte classes, however, its high volatility limits acquisition times of MALDI time-of-flight (TOF) experiments [13].

Biological application or technological advancement of MALDI IMS for lipid analysis has been performed in numerous studies. Advancements include development of tissue washing protocols, new chemical matrices, and matrix application methods [26–35]. The most thorough studies to investigate MALDI matrices for IMS have focused on DAN, investigating analyte sensitivity and degradation patterns [12, 36]. However, these studies concentrated on a single matrix or utilized instrumental platforms with limited molecular coverage, restricting the number of observed lipids.

Herein, the relative sensitivity and molecular coverage of commonly employed MALDI matrices is compared for IMS of lipids. This systematic assessment leverages high resolving

power Fourier transform ion cyclotron resonance (FT-ICR) IMS to evaluate lipid profiles with exceptional molecular coverage and specificity. Comparisons of IMS datasets collected using various MALDI matrices elucidate trends in observed lipid sub-class and adduct formation. We note the propensity of DAN to modify phosphatidylcholine lipids during negative ion mode IMS analysis as well as differences in adduct formation in positive ion mode IMS analysis. Evaluation of the effective sensitivity and molecular coverage of lipid sub-classes will enable more informed experimental design for IMS experiments.

Methods

Materials

2,5-dihydroxyacetophenone (DHA, 97%), 1,5-diaminonaphthalene (DAN, 97%), 5-chloro-2-mercaptobenzothiazole (CMBT, 90%), 2,5-dihydroxybenzoic acid (DHB, 98%), ammonium formate, hematoxylin, and eosin were purchased from Sigma Aldrich (St. Louis, MO, USA). Matrices were purified by recrystallization. 9-aminoacridine free base (9AA) was purchased from Santa Cruz Biochem (Dallas, TX, USA). Indium tin oxide (ITO) coated slides were purchased from Delta Technologies, Limited (Loveland, CO). All solvents (methanol, ethanol, acetonitrile, trifluoroacetic acid, xylenes, and acetone) and optimal cutting temperature compound were purchased from Fisher Scientific (Kalamazoo, MI, USA).

Sample Preparation

Fresh frozen mouse liver tissue (n=1 animal) was serially sectioned at 12 μm thickness using a Leica CM3050s cryostat (Leica Biosystems, Buffalo Grove, IL, USA) and thaw mounted on ITO coated glass slides (Delta Technologies, Loveland, CO, USA). Sections were stored at −80 °C until thawed under vacuum. MALDI matrix was primarily applied by a robotic aerosol sprayer (TM Sprayer, HTX Technologies, Chapel Hill, NC, USA) using optimized conditions: 9AA in 90% methanol: 10% ddH_2O at 85°C, CMBT in 90% acetone: 10% ddH_2O at 30°C, DAN in 90% acetonitrile: 10% ddH_2O at 85°C, DHA in 90% acetonitrile: 9.9% ddH_2O: 0.1% trifluoroacetic acid at 85°C, and DHB in 70% methanol: 30% ddH_2O at 85°C. The amount of matrix per unit area of sprayed matrices are as follows: 9AA at 3.1 $\mu g/mm^2$, CMBT at 18.0 $\mu g/mm^2$, DAN at 3.6 $\mu g/mm^2$, DHA at 3.1 $\mu g/mm^2$, and DHB at 1.3 $\mu g/mm^2$. More information on matrix application by robotic aerosol sprayer can be found in Table S1. For matrix application comparisons, matrix was sublimed onto tissue sections using a custom built sublimation apparatus [36]. Sublimation was performed using approximately 300 mg of DAN at 130°C and 25 mTorr vacuum for a final coating density of 2.0 $\mu g/mm^2$ and approximately 300 mg of DHA at 110°C and 25 mTorr vacuum for a final coating density of 2.0 $\mu g/mm^2$. Amount of sublimated matrix per unit area was calculated by measuring the weight differential and coated area. Post-imaging, sections underwent a methanol wash to remove matrix followed by hematoxylin and eosin (Fisher Scientific, Kalamazoo, MI, USA) staining. Stained sections were scanned for visualization using a Leica SCN 400 optical slide scanner (Leica Microsystems GmbH, Wetzlar, Germany) at 20X magnification.

Data Acquisition

All experiments were performed using a 15T FT-ICR mass spectrometer (MS) (solariX, Bruker Daltonics, Billerica, MA, USA) equipped with an Apollo II dual MALDI/ESI source and an infinity cell (Bruker Daltonics, Billerica, MA, USA). The MALDI source employs a smartbeam II 2 kHz, frequency tripled Nd:YAG (355 nm) laser. Molecular images were acquired with a pitch of 300 μm in both the *x* and *y* directions using a ~50 μm laser beam size (250 to 1500 laser shots). Laser fluence was adjusted for each sample to achieve optimal analyte signals. IMS data were acquired in both polarities from *m/z* 300 – 2000 with a resolving power (*m/Δm*) of ~ 330,000 at *m/z* 400. An x,y pitch offset of 150 μm allowed IMS data acquisition of both polarities from each prepared tissue sample. The time domain file size was set to 2M (free induction decay: 1.15 s). The ion optics were tuned to maximize transmission at the defined *m/z* range including the funnel RF amplitude (220 V_{pp}), source octopole (5 MHz, 310–360 V_{pp}), collision cell (collision cell voltage: +/− 2–3 V, cell: 2 MHz, 800–1000 V_{pp}), time-of-flight delay (0.7– 0.8 ms), transfer optics (4 MHz, 380 V_{pp}), and quadrupole (Q1 mass: *m/z* 550–700) for each matrix used. In-source collision-induced dissociation was introduced when necessary to reduce matrix clusters. The source DC optics were also tuned to maximize signal (capillary exit +/− 260 V, deflector plate: +/− 200 V, plate offset: +/− 80 V, funnel 1: +/− 110–180 V, skimmer 1: +/− 15–35 V) as well as the ICR cell parameters (transfer exit lens: +/− 15 V, analyzer entrance: +/− 1.5 V, side kick: 0 V, side kick offset: +/− 6–9 V, and front and back trap plates: +/− 1.0–1.5 V). Ion detection was performed using a sweep excitation power of 18%. Data were calibrated externally using red phosphorous clusters prior to analysis and calibrated internally post-acquisition in FTMS Processing software (Bruker Daltonics, Billerica, MA, USA) using known lipid species as lock mass assignments. Data were acquired in triplicate for each MALDI matrix. Hematoxylin and eosin (H&E) stained bright field images of the tissue sections were overlaid with IMS data and imported into SCiLS Lab software (version 2016b, SCiLS GmbH, Bruker Daltonics) for visualization and analysis.

Data Analysis

Data from lipid measurements were analyzed using SCiLS Lab 2016b (Bruker Daltonics, Billerica, MA, USA) (Fig. S1). Unsupervised analyses consisted of spatial segmentations and principal component analysis (PCA). Bisecting k-means spatial segmentation was applied to all acquired data to identify off-tissue spectra containing only matrix signal in order to remove them from consideration for analysis. Following segmentation, positive and negative ion mode datasets were separately subjected to PCA with three components for multivariate comparison. For supervised analyses, peak filter lists were created from *m/z* values corresponding to lipid species derived from LIPID MAPS database (The LIPID MAPS Lipidomics Gateway, http://www.lipidmaps.org/) and imported into SCiLS Lab software. Peak interval windows were created from values +/− 0.009% (~18 ppm) of each *m/z* value for $[M+H]^+$, $[M+Na]^+$, $[M+K]^+$, and $[M-H]^-$ potential ion types. Percentage-based intervals appropriately scale increasing *m/z* values with decreasing instrumental mass resolution. Peak filter lists allowed rapid molecular annotation of any intensity value (filtered to signal-to-noise ratio > 3) present within an interval. Although the wider mass interval windows can provide false positives for chemical annotation, the high resolving power (>300,000 at m/z 750) and recalibrated mass accuracy (<3 ppm) of the FT-ICR MS data

limit these occurrences [38]. However, it is noted that this approach does not account for isomeric species. All molecular identifications are tentative and based on accurate mass measurements. Receiver operating characteristic (ROC) analyses of the annotated intensities from the LIPIDMAPS interval list were performed by comparing data replicates (n=3 analyses per MALDI matrix) from one matrix in a single class to replicates from all other experimental groups. Structuring the ROC analyses in this manner isolated differences in lipid intensities and frequencies unique to a single MALDI matrix when compared to other matrices. Area under the ROC curve (AUC) values for each interval were exported for the generation of heat maps using the open source *R* environment or Microsoft Excel. AUC values measure the discrimination quality of a single signal between two distributions (sets of matrix-associated IMS pixels in this instance). A value of 1.0 or 0 would indicate perfect discrimination between two classes. Color gradients were applied to AUC values within each heat map. These AUC color gradients allow visualization of the corresponding frequency and abundance of a variety of lipid species from any experimental condition. In heat maps displaying only lipid sub-class rather than specific lipid species, AUC values were averaged for all lipid species in a class and color gradients were assigned based on percentiles. Ion images were generated for specific *m/z* values highlighted by statistical analyses to visually confirm findings. Ion images provided visual context of the trends identified by the analyses.

Results & Discussion

Matrix Effects on Positive Ion Mode Lipid Analysis

Visual comparison of IMS averaged spectra show differences in spectral profiles for each matrix tested (Fig. 1a). In the lower *m/z* range (*m/z* 300 – 550), higher intensity signals resulting from matrix clusters can be observed in the DAN averaged spectrum relative to other matrices. CMBT, uniquely, produced matrix-lipid adducts that can be observed from *m/z* 1,000– 1,100 (fragmentation data not shown). Signals from *m/z* 1,500 – 1,650, observed in all cases, were determined to be lipid dimer species based on mass accuracy measurements. Although dimer signals visually appear less intense with CMBT matrix, this is an effect of scaling due to high intensity signals from *m/z* 1,000 – 1,100. Lipid sub-classes, compared as a percent composition of the total number of lipids for protonated, sodiated, and potassiated ion types, generally show similar profiles for the matrices tested. (Fig. 1b – 1d). However, several trends were elucidated for each of the common cation adducts. For $[M+H]^+$ ion types (Fig. 1b), the highest percentage of phosphatidylglycerols (purple) was detected using DHA. Additionally, DAN resulted in a higher relative percentage of glycophospholipids (light green), whereas the highest percentage of phosphatidylserines was detected using 9AA (dark purple). The highest percentage of sodiated sulfatides (dark orange) was detected using DAN, and the highest percentage of sodiated phosphatidylethanolamines (dark blue) was detected using DHA (Fig. 1c). Finally, the relative percentage of potassiated cardiolipins (yellow) and potassiated glycerophospholipids (green) were higher for all matrices compared to protonated and sodiated ion types (Fig. 1d). To compare sensitivity and propensity for adduct formation, the total number of lipids was compared for each ion type (Fig. 1e). While the largest number of lipids were detected with DHA, many were $[M+Na]^+$ ion types. Although DAN is highly

sensitive it does not provide the molecular coverage of 9AA, CMBT, and DHA. These comparisons show broad differences in observed intensities when employing various matrices for IMS of lipids. However, specific trends in positive ion mode data can be further isolated using statistical tools such as PCA and ROC analysis.

PCA of positive ion mode IMS data differentiated each of the five MALDI matrices tested. (Fig. 2). The scores plot from component 1 and component 2 account for 83.0% of the total variance of the dataset. Qualitatively, most of the differentiation between the spectral profiles of the MALDI matrices is captured in the first principal component. CMBT, DHA, and DHB positive ion mode data have the most similar spectral profiles, while data acquired using 9AA and DAN have overlapping profiles that are clearly distinguishable from the other matrices (Fig. 2a). The loadings plot from these data highlights ions that are primary contributors of variation across datasets and can be used to further probe specific molecular differences. Fig. 2b shows many data points corresponding to specific ions, distant from the central data cluster. Ions located outside of the 95% confidence interval were identified as predominately phosphatidylcholines. Most phosphatidylcholines to the left of the central cluster are cationized by potassium, while most phosphatidylcholines right of the central data cluster are protonated. This insight suggests that there is a large difference in the adducts formed during ionization for each MALDI matrix.

Heat maps allow visualization of data from binary, supervised ROC analyses based on intensity and frequency for specific lipid sub-classes and allow for interpretation of sensitivity differences within these complex datasets (Fig. 3). ROC analyses were structured to isolate differences in annotated lipid intensities and frequencies unique to a single MALDI matrix when compared to other matrices. Data acquired using 9AA have higher sensitivity for protonated and sodiated phosphatidylserines relative to other matrices. CMBT, DHA and DHB show similar relative lipid sub-class sensitivities for protonated species including higher sensitivity for phosphatidylglycerols and sulfatides. CMBT, DHA and DHB matrices also displayed lower sensitivity for protonated phosphatidylserines and phosphatidylcholines, and higher sensitivity for sodiated phosphatidylcholines. Data acquired using 9AA and DAN have a higher sensitivity for protonated phosphatidylcholines. Finally, DHA resulted in higher sensitivity for potassiated signals of all lipid classes when compared to other matrices.

To determine the effect of sample preparation on the ion type observed in IMS, matrix spray coating was compared to sublimation with and without a washing protocol to remove endogenous salts from the tissue. Heat maps for protonated, sodiated, and potassiated lipid annotations are shown for robotically sprayed and sublimated matrix application methods (with and without washing with 1 mM ammonium formate, Fig. 4) [13, 26]. DHA shows a higher propensity to form potassiated and sodiated ion types when applied using a robotic aerosol sprayer, presumably due to salts being introduced during the spraying process. When matrix is applied by sublimation, potassiated and sodiated adducts are reduced. When tissues are washed with an ammonium formate buffer followed by sublimation of the matrix, protonated lipid ion types dominate the spectra. This is consistent with previous work showing matrix application and tissue washing methods having an effect on adduct

formation due to the presence of nonvolatile salts, either endogenous to tissue or introduced by robotic aerosol sprayer matrix application [26, 39].

Lipid images of liver tissues collected as part of the statistical analyses highlighted above are depicted in Fig. 5. Liver tissue was selected for IMS analysis due to its homogenous morphology. Three protonated phosphatidylcholines for each matrix are shown in Fig. 5a. These ion images display higher abundances in the 9AA and DAN datasets. Three phosphatidylcholines with potassium adducts are shown in Fig. 5b. These ion images display higher intensities in the CMBT, DHA, and DHB datasets. The images visually confirm findings from the positive ion mode AUC heat maps, showing differential formation of protonated, sodiated, or potassiated adducts based on the selected MALDI matrix.

Matrix Effects on Negative Ion Mode Lipid Analysis

Negative ion mode IMS lipid analysis predominately results in deprotonated ion types [38]. Similar analytical strategies as those used for positive ion mode analysis were used to assess negative ion mode lipid IMS data. Visual comparison of averaged IMS spectra (Fig. 6a) show significant differences in spectral profiles. A grouping of high intensity signals can be observed from *m/z* 700–800 when using DAN. Annotation of these lipids based on accurate mass measurements alone suggests that phosphatidylethanolamines are detected with greater sensitivity using DAN relative to other MALDI matrices. Additionally, the propensity of each matrix to produce chemical noise (*i.e.* matrix clusters) in the low *m/z* range (*m/z* values < 500) varies dramatically. For example, matrix-related peaks are far more intense than lipid signals when using DHB in negative ion mode. The number of lipid annotations from each sub-class was compared as a percentage of the total number of annotated lipid species for deprotonated ion types (Fig. 6b). DHB produced the fewest number of total annotated lipids (Fig. 6c) predominately comprised of cardiolipins (yellow), glycosphingolipids (green), phosphatidylinositols (pink), and phosphatidylserines (dark purple). Similar species were observed for all other matrices tested. However, DAN showed a significant increase in the number of annotated phosphatidylethanolamines relative to the other lipid sub-classes. Overall, DAN and 9AA produced the largest number of deprotonated lipid ions detected in negative ion mode. This increased efficiency in negative ion mode by 9AA and DAN is attributed to the gas phase basicity or proton affinity inherent to the matrices. To further dissect trends within negative ion mode data, PCA and ROC analysis were employed.

PCA of the negative ion mode data provides a global view of the molecular variance between the MALDI matrices. The scores plot for principal components 1 and 2, accounting for 65.2% of the total variance of the dataset, shows that DHB and DAN datasets lie partially outside of the 95% confidence interval and distant from data acquired using 9AA, CMBT, and DHA (Fig. 7a). The negative ion mode loadings plot (Fig. 7b) separates the ions into three areas outside of the 95% confidence interval ellipse. In addition to matrix clusters, there are many annotated phosphatidylethanolamines distant from the 95% confidence interval ellipse suggesting these ions play a large role in the observed variance between the examined matrices. This observation was confirmed when analyzing the heat maps for specific lipid sub-classes (Fig. 8). A high AUC value can be observed for

phosphatidylethanolamines within the DAN matrix dataset compared to other negative ion mode data acquired using other matrices.

A significant driver of this apparent sensitivity for phosphatidylethanolamines is due to lipid modifications induced by DAN during the desorption/ionization process [19]. Typically, phosphatidylcholines are not observed in negative mode analysis due to the fixed positive charge on the choline head group. However, when performing negative ion mode MALDI MS analysis of lipids using DAN, a methyl group is lost from the head group of phosphatidylcholines. This loss enables efficient ionization in negative ion mode (Supp. Fig. 9). It is hypothesized that an amide group from the DAN matrix molecule interacts with a choline head group during the MALDI process, resulting in the creation of a 2-methyl amino head group (2MeN). The *m/z* values corresponding to phosphatidylcholines modified in this way are isomeric with phosphatidylethanolamines comprised of two additional carbons in the fatty acyl chains. These modified lipids are often misidentified and introduce experimental bias when employing DAN as a MALDI matrix to analyze complex lipid mixtures in negative ion mode.

Ion images generated from signals highlighted by negative ion mode statistical analyses are shown in Fig. 9. Ion images shown in Fig. 9a correspond to molecular species less abundant in DAN data matrix. Alternatively, Fig. 9b shows ion images for a phosphatidylinositol, PI(38:4), detected using all matrices and two examples of phosphatidylcholines that have been modified during MALDI with DAN (2MeN-PE(36:4) and 2MeN-PE(36:6)).

Conclusions

The sensitivity of commonly employed MALDI matrices for the analysis of lipids was compared using IMS. A global view of similarities and differences was achieved through both qualitative and quantitative approaches. Visual comparison of spectral data offered insight into the most abundant ions for each matrix (lipids, matrix clusters, or matrix-lipid adducts). The total number of lipids detected and differences between the relative number of species associated with each lipid sub-class were compared. PCA and ROC analyses enabled examination of intensity-related trends within the data. These analyses uncovered dissimilarity in the relative sensitivity for lipid sub-classes and propensity to generate sodiated and potassiated lipid cations. Of note, DAN and 9AA showed a higher propensity for producing protonated ions whereas other matricies tested (DHB, DHA and CMBT) were more highly sensitive for sodiated and potassiated lipid cations. In negative ion mode, a major finding was that DAN produced lipid profiles that were significantly different than the other matrices tested. This was found to result from modification of the head group of phosphatidylcholines during desorption/ionization. An assessment of common lipid matrices uncovered chemical phenomena attributed to the method of sample preparation, adduct formation, or analyte modification that should be considered when performing MALDI IMS of lipids. The depth of analysis provided by this study allowed for insight into data trends that can indicate potential experimental biases. Furthermore, the data analysis workflow highlighted here can serve as a general strategy for efficiently processing any IMS experiment where it is helpful to identify trends in global lipid measurements.

Supplementary Material

Refer to Web version on PubMed Central for supplementary material.

Acknowledgements

The authors would like to thank Marissa M. Jones for assistance creation of heat maps and Drs. Mark Boothby and Sung Hoon Cho for providing the mouse liver tissue. Animals were used and handled in accordance with protocols approved by the Vanderbilt University Institutional Animal Care and Use Committee (IACUC). Support for this work is provided by the NIH: National Institute of General Medical Sciences (5-P41 GM103391-08 (R.M.C.)), National Institute of Allergy and Infectious Diseases (R01AI138581 (J.M.S)), National Institute of Diabetes and Digestive and Kidney Diseases (U54DK120058 (J.M.S. and R.M.C.)), and the NIH Shared Instrumentation Grant Program (1S10OD012359-01 (R.M.C.)).

References

[1]. Hillenkamp F, et al.: Matrix-assisted laser desorption/ionization mass spectrometry of biopolymers. Anal. Chem 1991, 63(24), 1193A–1203A. [PubMed: 1897719]

[2]. Caprioli RM, Farmer TB, and Gile J: Molecular imaging of biological samples: localization of peptides and proteins using MALDI-TOF MS. Anal. Chem 1997, 69(23), 4751–4760. [PubMed: 9406525]

[3]. Caprioli RM: Imaging mass spectrometry: molecular microscopy for enabling a new age of discovery. Proteomics. 2014, 14(7–8), 807–809. [PubMed: 24497141]

[4]. McDonnell LA and Heeren RMA: Imaging mass spectrometry. Mass Spectrom Rev. 2007, 26(4), 606–643. [PubMed: 17471576]

[5]. Patterson NH, et al.: Co-registration and analysis of multiple imaging mass spectrometry datasets targeting different analytes. Bioinformatics. 2018, bty780–bty780.

[6]. Wyatt MF, Stein BK, and Brenton AG: Characterization of various analytes using matrix-assisted laser desorption/ionization time-of-flight mass spectrometry and 2-[(2E)-3-(4-tert-Butylphenyl)-2-methylprop-2- enylidene]malononitrile matrix. Anal. Chem 2006, 78(1), 199–206. [PubMed: 16383328]

[7]. Jaskolla T, et al.: The new matrix 4-chloro-α-cyanocinnamic acid allows the detection of phosphatidylethanolamine chloramines by MALDI-TOF mass spectrometry. J. Am. Soc. Mass Spectrom 2009, 20(5), 867–874. [PubMed: 19201617]

[8]. Wang J, et al.: MALDI-TOF MS imaging of metabolites with a N-(1-naphthyl) ethylenediamine dihydrochloride matrix and its application to colorectal cancer liver metastasis. Anal. Chem 2015, 87(1), 422–430. [PubMed: 25474421]

[9]. Fukuyama Y, et al.: Alkylated trihydroxyacetophenone as a MALDI matrix for hydrophobic peptides. Anal. Chem 2013, 85(20), 9444–9448. [PubMed: 24063356]

[10]. Yang J, Norris JL, and Caprioli R: Novel vacuum stable ketone-based matrices for high spatial resolution MALDI imaging mass spectrometry. J. Mass Spectrom 2018, 53, 1005–1012. [PubMed: 30073737]

[11]. Calvano CD, et al.: MALDI matrices for low molecular weight compounds: an endless story? Anal. Bioanal. Chem 2018, 410(17), 4015–4038. [PubMed: 29682685]

[12]. Thomas A, et al.: Sublimation of new matrix candidates for high spatial resolution imaging mass spectrometry of lipids: enhanced information in both positive and negative polarities after 1,5-diaminonapthalene deposition. Anal. Chem 2012, 84(4), 2048–2054. [PubMed: 22243482]

[13]. Zavalin A, et al.: Tissue protein imaging at 1 μm laser spot diameter for high spatial resolution and high imaging speed using transmission geometry MALDI TOF MS. Anal. Bioanal. Chem 2015, 407(8), 2337–2342. [PubMed: 25673247]

[14]. Armstrong DW, et al.: Ionic liquids as matrixes for matrix-assisted laser desorption/ionization mass spectrometry. Anal. Chem 2001, 73(15), 3679–3686. [PubMed: 11510834]

[15]. Beavis RC, Chaudhary T, and Chait BT: Alpha-cyano-4-hydroxycinnamic acid as a matrix for matrix-assisted laser desorption mass spectrometry. Organic Mass Spectrom. 1992, 27(2), 156–158.

[16]. Strupat K, Karas M, and Hillenkamp F: 2,5-Dihyroxybenzoic acid - a new matrix for laser desorption ionization mass spectrometry. Int. J. Mass Spectrom 1991, 111, 89–102.

[17]. Xu NX, et al.: Mercaptobenzothiazoles: A new class of matrices for laser desorption ionization mass spectrometry. J. Am. Soc. Mass Spectrom 1997, 8(2), 116–124.

[18]. Vermillion-Salsbury RL and Hercules DM: 9-aminoacridine as a matrix for negative mode matrix-assisted laser desorption/ionization. Rapid Commun Mass Spectrom. 2002, 16(16), 1575–1581.

[19]. Schröter J, et al.: The combination of 2,5-dihydroxybenzoic acid and 2,5-dihydroxyacetophenone matrices for unequivocal assignment of phosphatidylethanolamine species in complex mixtures. Anal. Bioanal. Chem 2018, 410(9), 2437–2447. [PubMed: 29445834]

[20]. Schiller J, et al.: The suitability of different DHB isomers as matrices for the MALDI-TOF MS analysis of phospholipids: which isomer for what purpose? Eur. Biophys. J 2007, 36(4), 517–527. [PubMed: 17047951]

[21]. Groseclose MR and Castellino S: A mimetic tissue model for the quantification of drug distributions by MALDI imaging mass spectrometry. Anal. Chem 2013, 85(21), 10099–10106. [PubMed: 24024735]

[22]. Li S, et al.: Electrospray deposition device used to precisely control the matrix crystal to improve the performance of MALDI MSI. Sci. Rep 2016, 6, 37903. [PubMed: 27885266]

[23]. Gemperline E, Rawson S, and Li L: Optimization and comparison of multiple MALDI matrix application methods for small molecule mass spectrometric imaging. Anal. Chem 2014, 86(20), 10030–10035. [PubMed: 25331774]

[24]. Fuchs B, et al.: Phosphatidylcholines and -ethanolamines can be easily mistaken in phospholipid mixtures: a negative ion MALDI-TOF MS study with 9-aminoacridine as matrix and egg yolk as selected example. Anal. Bioanal. Chem 2009, 395(8), 2479. [PubMed: 19690837]

[25]. Korte AR & Lee YJ: MALDI-MS analysis and imaging of small molecule metabolites with 1,5-diaminonaphthalene (DAN). J. Mass Spectrom 2014, 49, 737–741. [PubMed: 25044901]

[26]. Angel PM, et al.: Enhanced sensitivity for high spatial resolution lipid analysis by negative ion mode matrix assisted laser desorption ionization imaging mass spectrometry. Anal. Chem 2012, 84(3), 1557–1564. [PubMed: 22243218]

[27]. Hankin JA, Barkley RM, and Murphy RC: Sublimation as a method of matrix application for mass spectrometric imaging. J. Am. Soc. Mass Spectrom 2007, 18(9), 1646–1652. [PubMed: 17659880]

[28]. Grove KJ, Frappier SL, and Caprioli RM: Matrix pre-coated MALDI MS targets for small molecule imaging in tissues. J. Am. Soc. Mass Spectrom 2011, 22(1), 192–195. [PubMed: 21472558]

[29]. Shanta SR, et al.: Binary matrix for MALDI imaging mass spectrometry of phospholipids in both ion modes. Anal. Chem 2011, 83(4), 1252–1259. [PubMed: 21244088]

[30]. Meriaux C, et al.: Liquid ionic matrixes for MALDI mass spectrometry imaging of lipids. J. Proteom 2010, 73(6), 1204–1218.

[31]. Astigarraga E, et al.: Profiling and imaging of lipids on brain and liver tissue by matrix-assisted laser desorption/ionization mass spectrometry using 2-mercaptobenzothiazole as a matrix. Anal. Chem 2008, 80(23), 9105–9114. [PubMed: 18959430]

[32]. Francese S, et al.: Curcumin: A multipurpose matrix for MALDI mass spectrometry imaging applications. Anal. Chem 2013, 85(10), 5240–5248. [PubMed: 23621442]

[33]. Stübiger G and Belgacem O: Analysis of lipids using 2,4,6-trihydroxyacetophenone as a matrix for MALDI mass spectrometry. Anal. Chem 2007, 79(8), 3206–3213. [PubMed: 17367115]

[34]. Cerruti CD, et al.: MALDI imaging and structural analysis of rat brain lipid negative ions with 9-aminoacridine matrix. Anal. Chem 2012, 84(5), 2164–2171. [PubMed: 22300189]

[35]. Fülöp A, et al.: 4-Phenyl-α-cyanocinnamic acid amide: screening for a negative ion matrix for MALDI-MS imaging of multiple lipid classes. Anal Chem. 2013, 85(19), 9156–9163. [PubMed: 23984824]

[36]. Patterson NH, Thomas A, and Chaurand P: Monitoring time-dependent degradation of phospholipids in sectioned tissues by MALDI imaging mass spectrometry. J. Mass Spectrom 2014, 49(7), 622–627. [PubMed: 25044847]

[37]. Yang J and Caprioli RM: Matrix sublimation/recrystallization for imaging proteins by mass spectrometry at high spatial resolution. Anal Chem. 2011, 83(14), 5728–34. [PubMed: 21639088]

[38]. Zemski Berry KA, et al.: MALDI imaging of lipid biochemistry in tissues by mass spectrometry. Chem. Rev 2011, 111(10), 6491–6512. [PubMed: 21942646]

[39]. Jaskolla TW, et al.: Comparison between vacuum sublimed matrices and conventional dried droplet preparation in MALDI-TOF mass spectrometry. J. Am. Soc. Mass Spectrom 2009, 20(6), 1104–1114. [PubMed: 19299165]

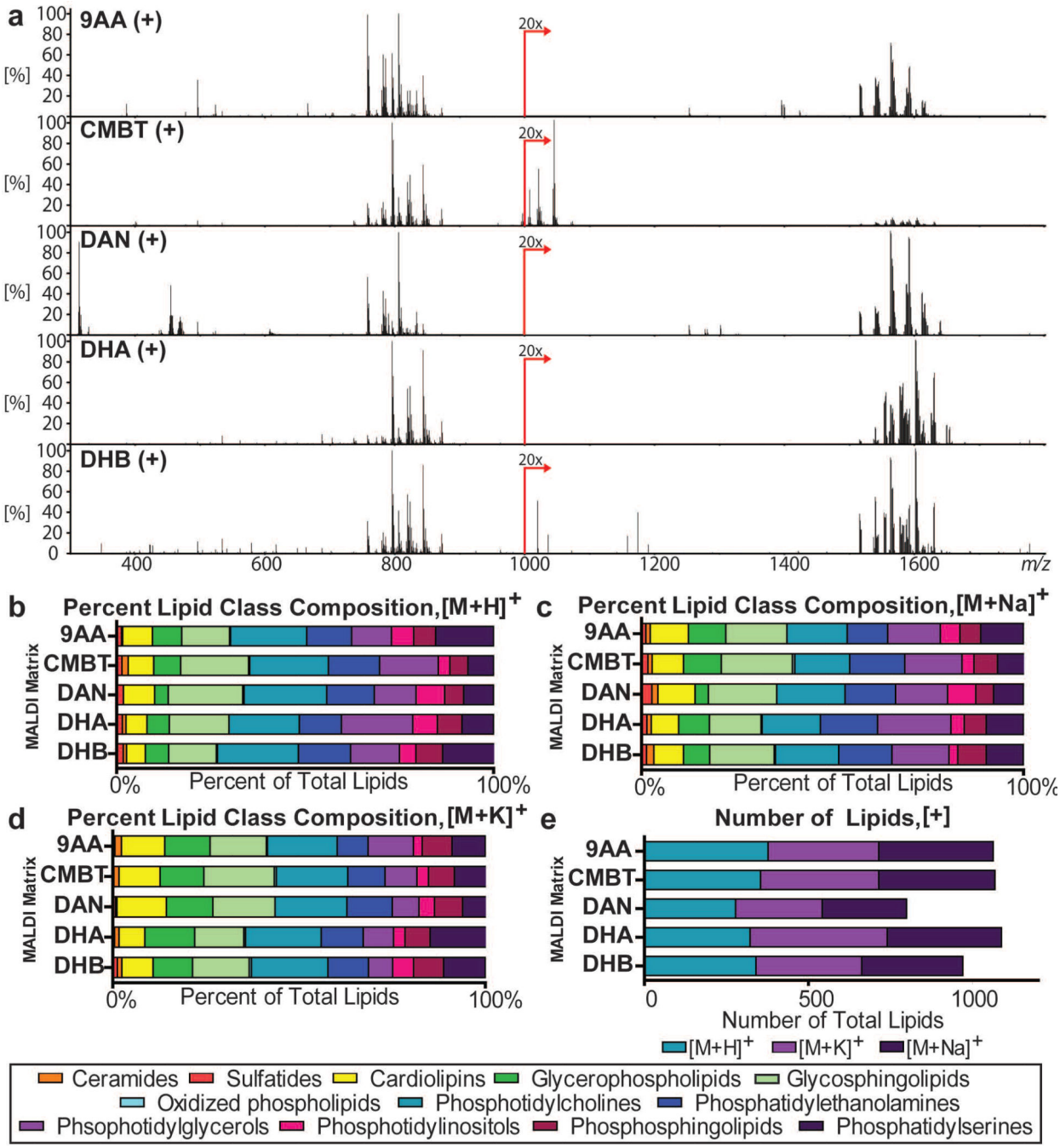

Figure 1: Comparisons of positive ion mode lipid analyses using several MALDI matrices reveal differences in global spectral profiles, the relative abundances of lipid sub-classes, and the lipid ion types.

a) The average spectra from the IMS analysis for 9AA, CMBT, DAN, DHA, and DHB matrices show differences in global spectral profiles. **b-d)** Lipids were aggregated into the appropriate lipid sub-classes and displayed as a percentage of the total number of lipids for the $[M+H]^+$, $[M+Na]^+$, and $[M+K]^+$ ion types. **e)** The total number of lipids was tabulated for each matrix and ion type to compare molecular coverage. The potential of a single lipid species forming multiple ion types was not accounted for.

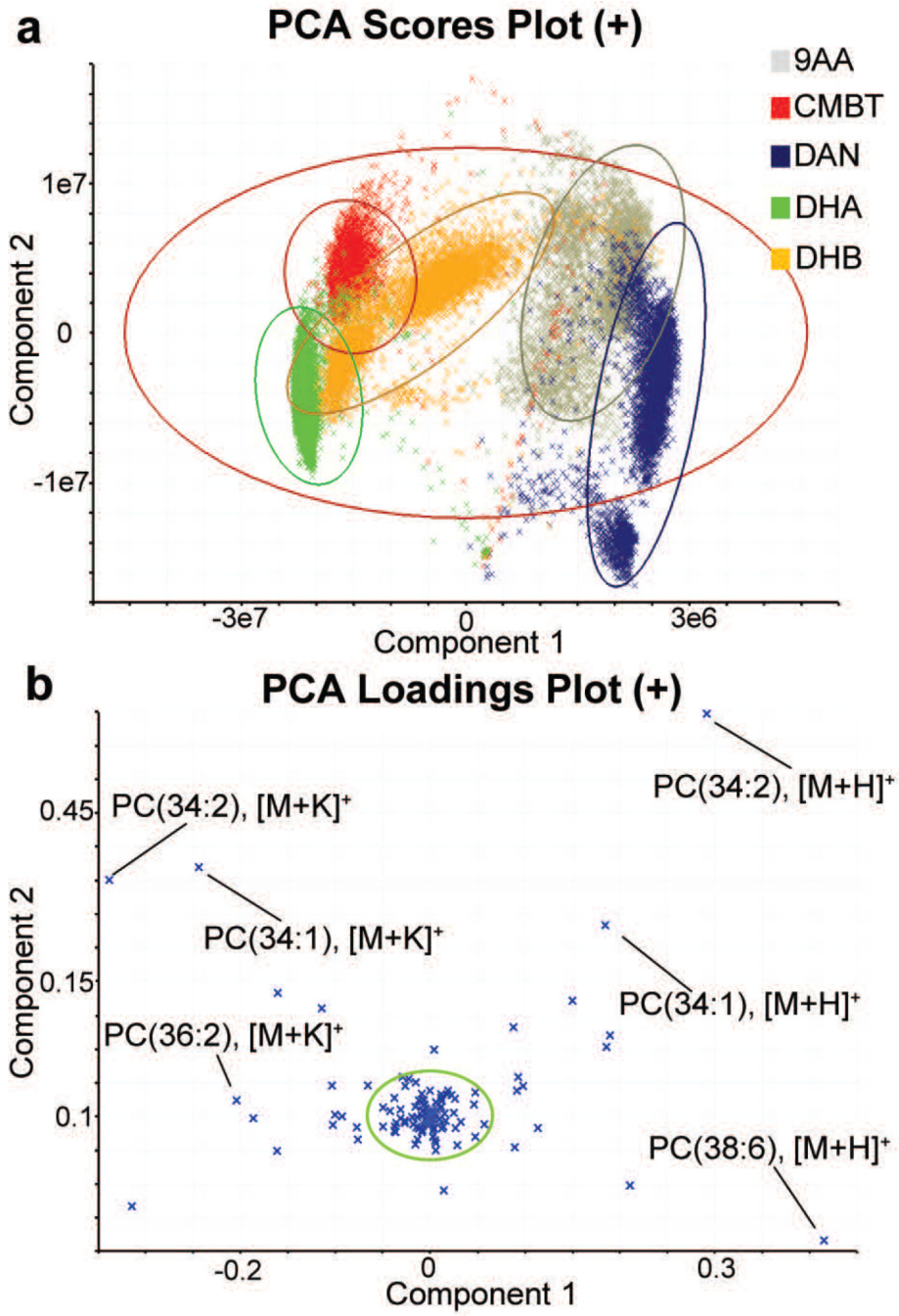

Figure 2: PCA elucidates qualitative differences among positive ion mode data.

a) A positive ion mode PCA scores plot with a 95% confidence ellipse reveals the variance of the data. **b)** A positive ion mode loadings plot with a 95% confidence ellipse highlights lipids that are separated from the central cluster, identified as protonated or potassiated phosphatidylcholines lipid species.

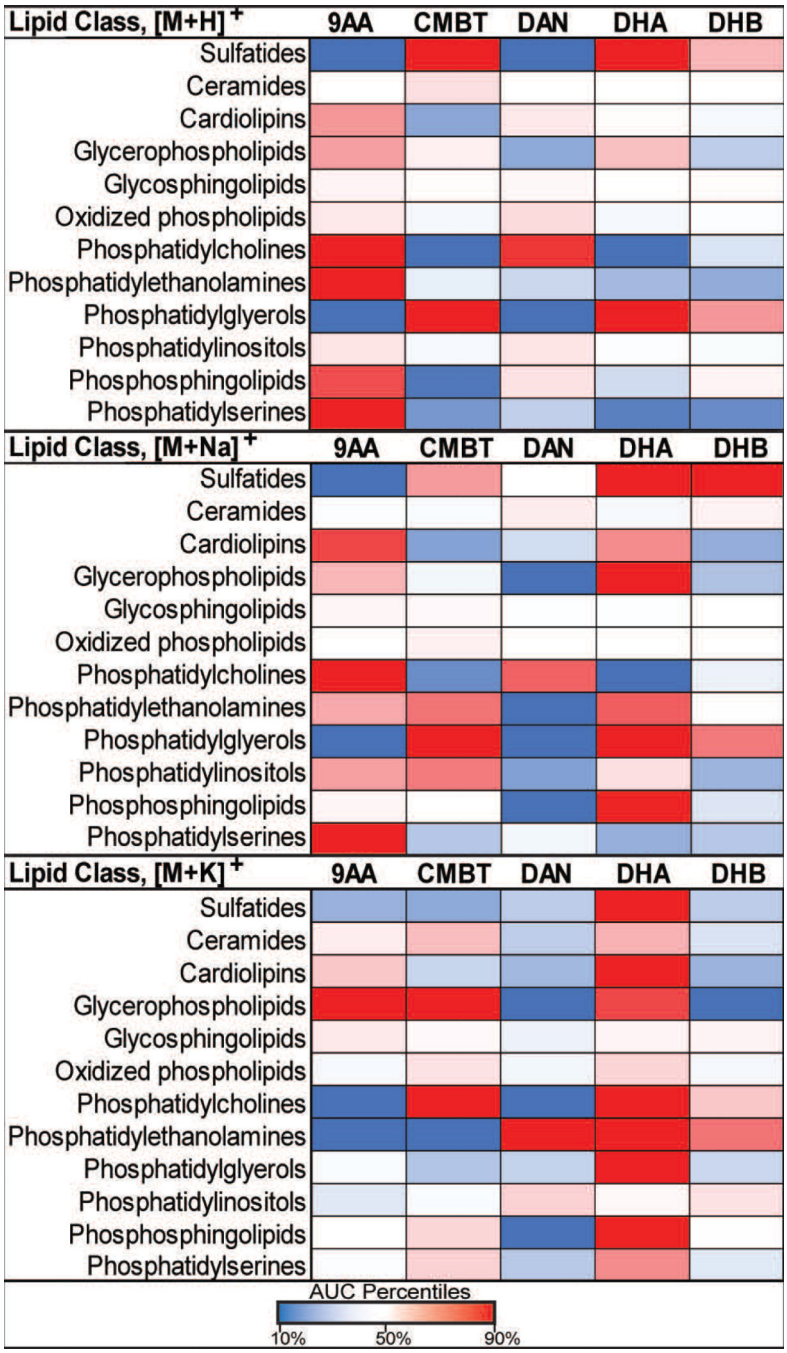

Figure 3: Positive ion mode heat maps for each lipid subclass allow for visualization of differences in sensitivity and are shown as a function of the ion type $[M+H]^+$, $[M+Na]^+$, and $[M+K]^+$.

Blue represents low abundance of a lipid sub-class and red represents a high abundance.

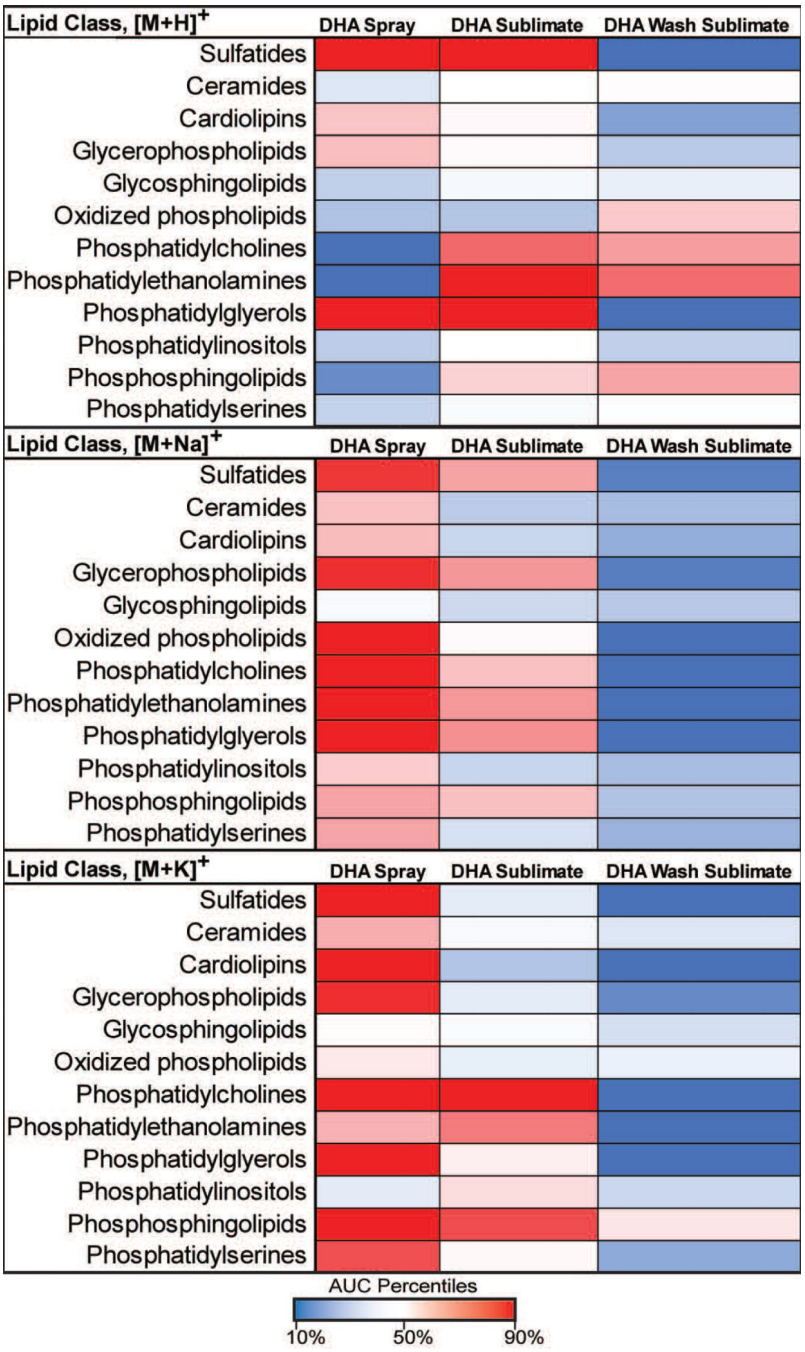

Figure 4: Heat maps for each lipid subclass allow for visualization of differences in sensitivity across $[M+H]^+$, $[M+Na]^+$, and $[M+K]^+$ ion types based on the DHA matrix application method.
Blue represents low abundance of a lipid sub-class and red is a high abundance.

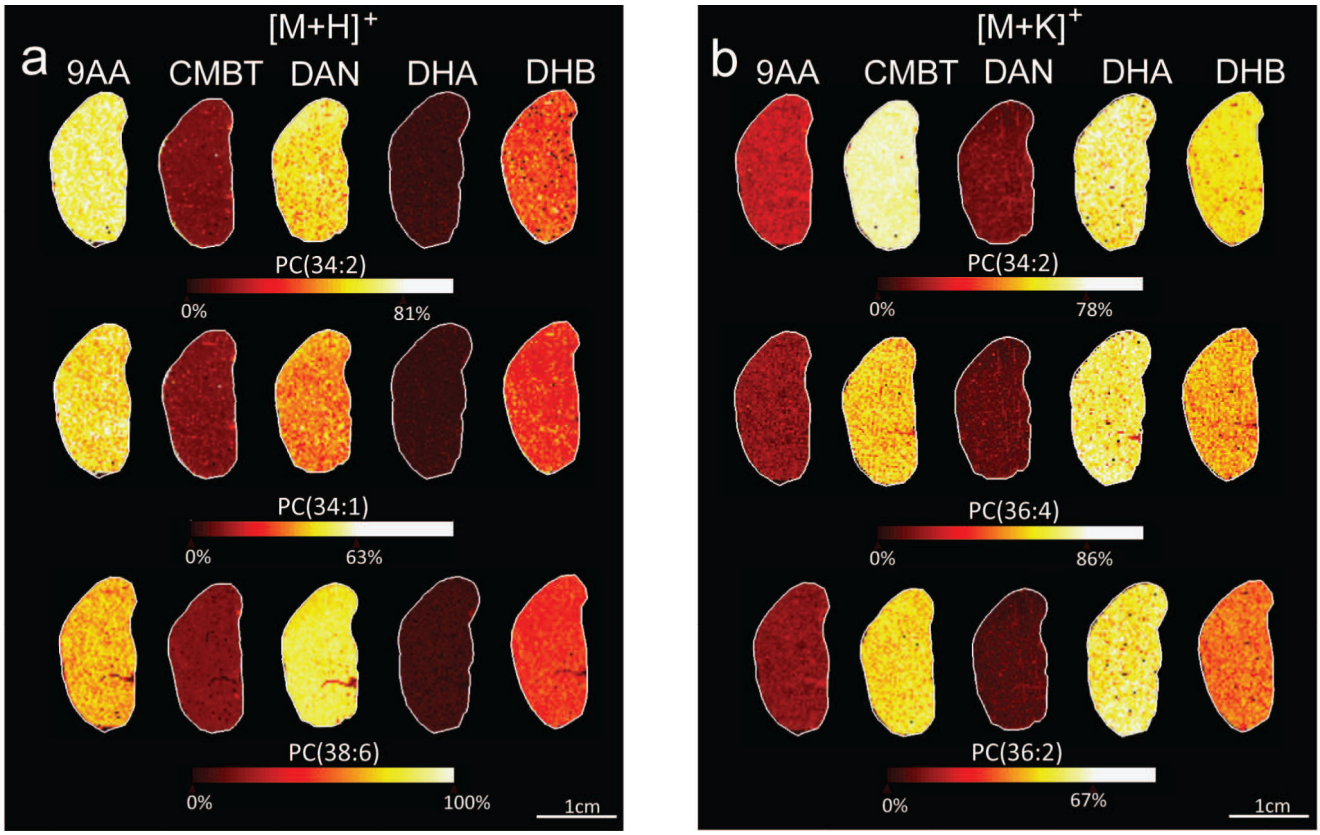

Figure 5: Individual lipid images generated from positive ion mode data.

a) Protonated PC ion types were found to be more abundant within 9AA and DAN datasets compared to other matrices. **b**) Potassium cationization was found to be more prevalent with CMBT, DHA, and DHB compared to 9AA and DAN.

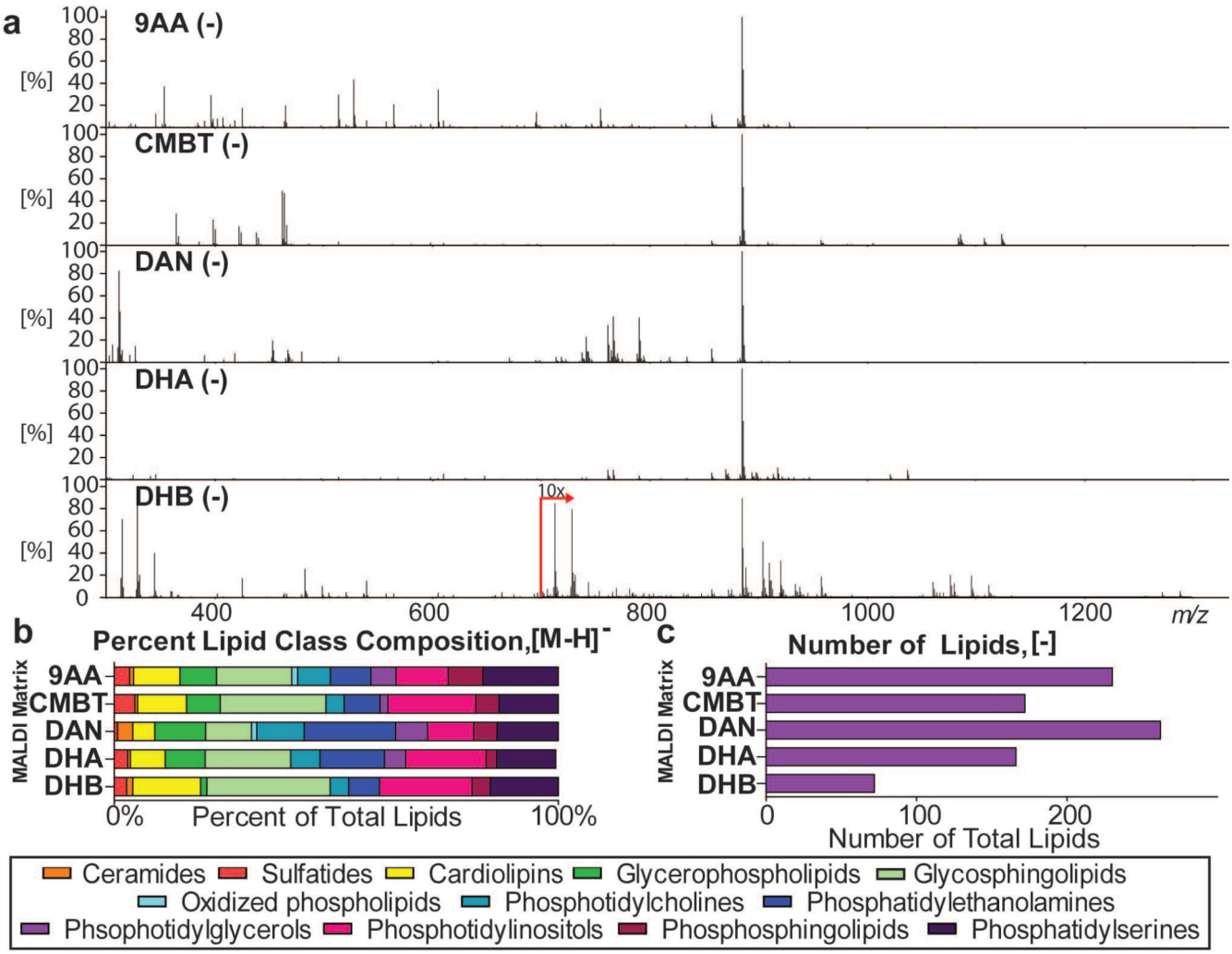

Figure 6: Comparisons of negative ion mode lipid analyses using several MALDI matrices reveal differences in global spectral profiles and the relative abundances of lipid sub-classes.

a) Averaged spectra from the IMS analyses for 9AA, CMBT, DAN, DHA, and DHB matrices show differences global spectral profiles. **b)** Lipids were aggregated into the appropriate lipid sub-classes, and displayed as a percentage of the total number of identified lipids. **c)** The total number of lipids was tabulated for each matrix to compare molecular coverage.

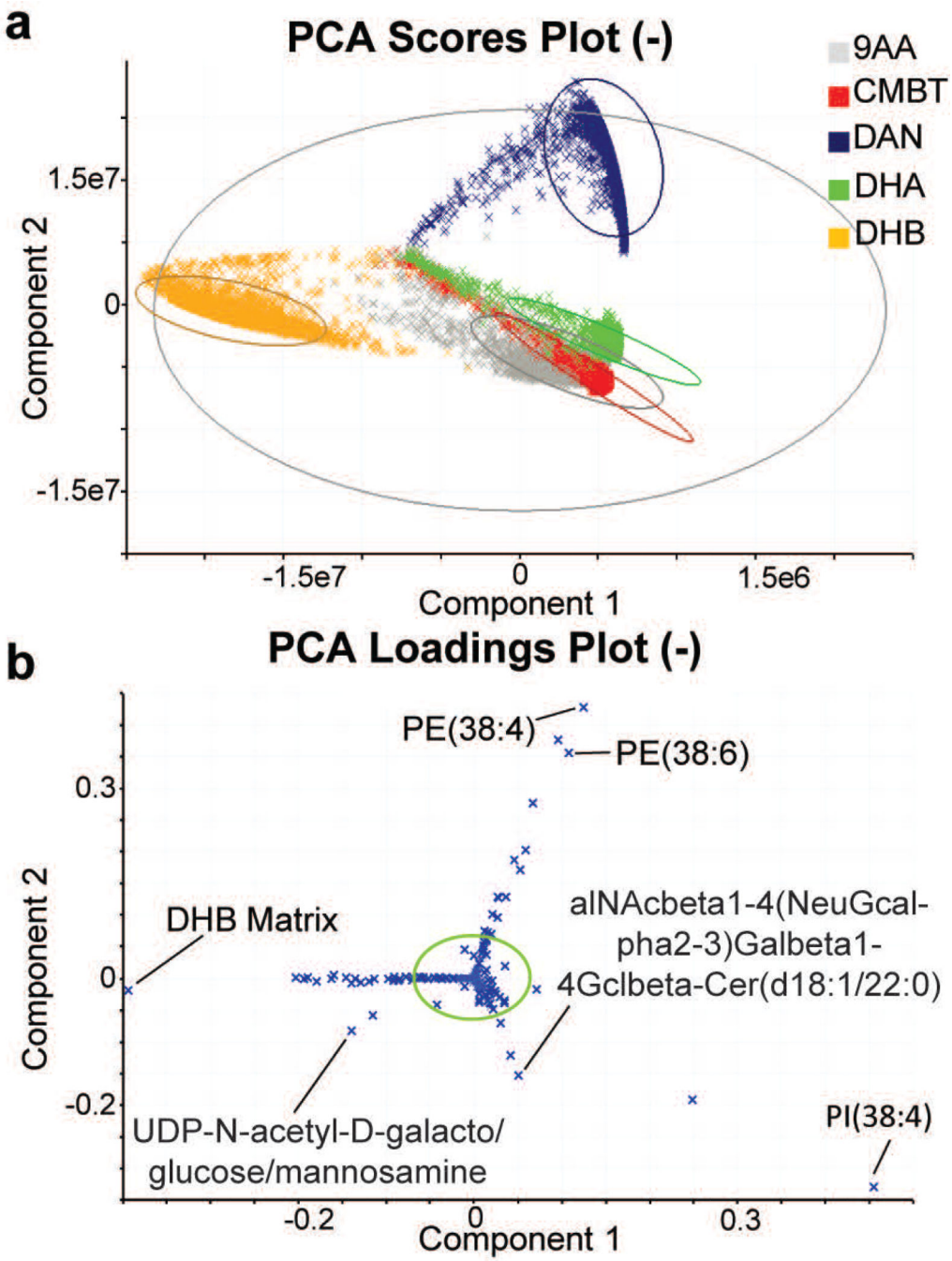

Figure 7: PCA elucidate differences among negative ion mode data.

a) A negative ion mode PCA scores plot with a 95th confidence ellipse reveals the variance of the data. **b)** A negative ion mode loadings plot with a 95th confidence ellipse highlights lipids that are separated from the central data cluster.

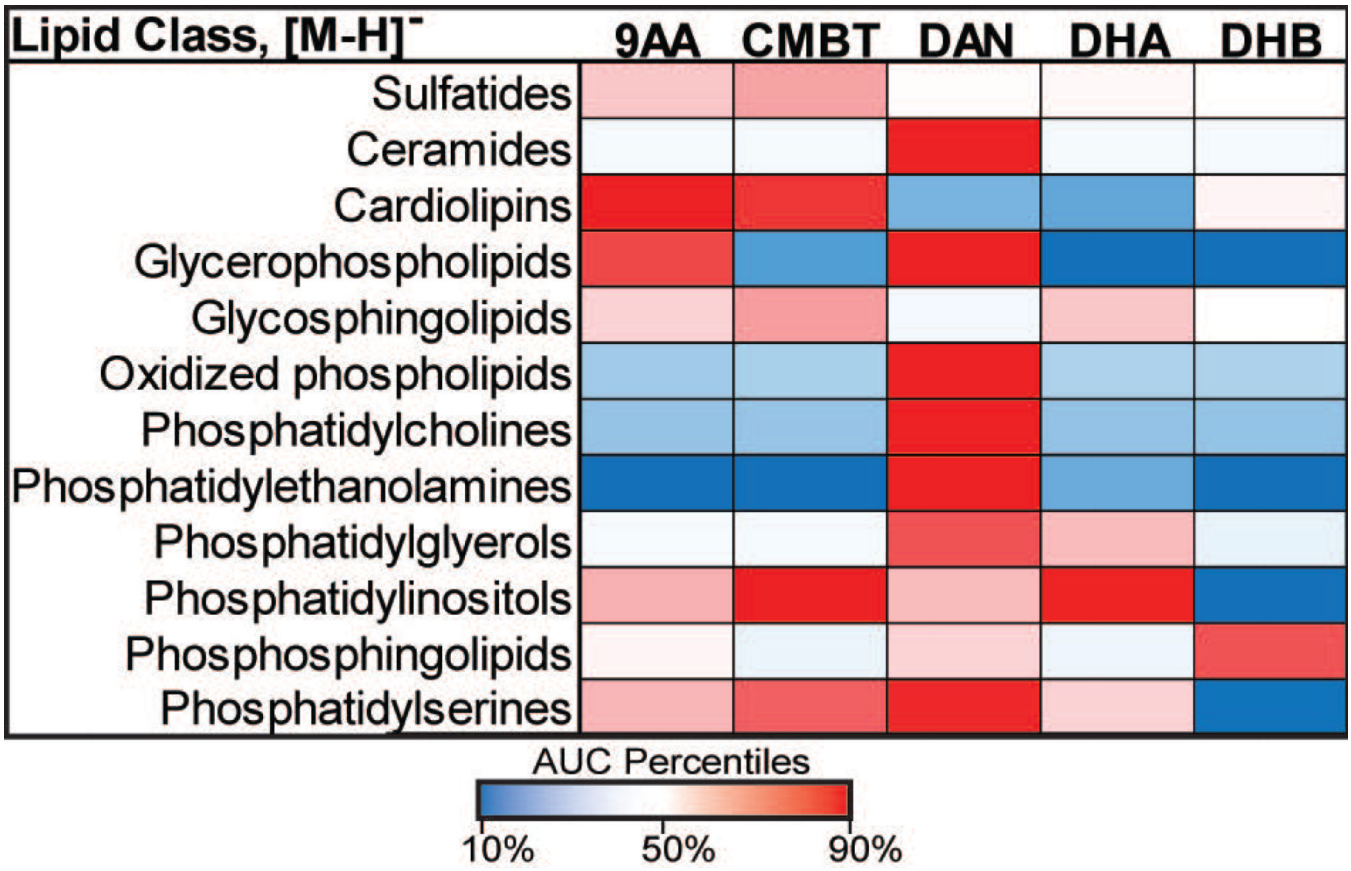

Figure 8: Negative ion mode heat maps for each lipid subclass allow for visualization of differences in sensitivity.

Blue represents low abundance of a lipid sub-class and red represents a high abundance.

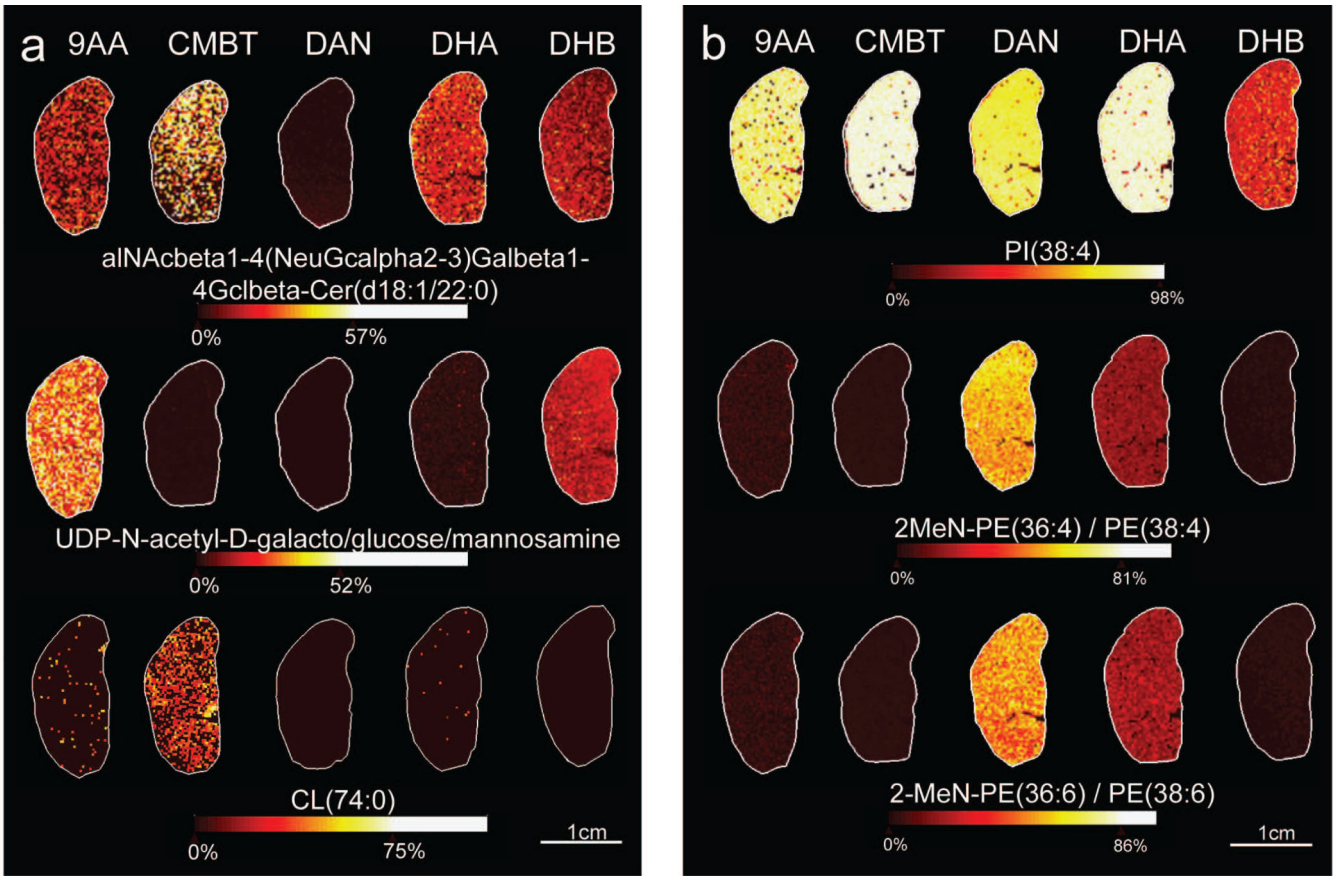

Figure 9: Individual lipid images generated from negative mode data provide visual context to trends.

(a) Many lipid sub-classes were found to be less abundant with DAN compared to the other four matrices. (b) However, multiple PE and PI lipids were found to be more abundant with DAN compared to the other four matrices.